ACS APPLIED ENERGY MATERIALS

Article

Cite This: ACS Appl. Energy Mater. 2019, 2, 3578−3586

www.acsaem.org

Interpreting Electrochemical and Chemical Sodiation Mechanisms and Kinetics in Tin Antimony Battery Anodes Using *in Situ* Transmission Electron Microscopy and Computational Methods

Jacob S. Gutiérrez-Kolar,[†] Loïc Baggetto,[‡] Xiahan Sang,[§] Dongwon Shin,[∥] Vitaliy Yurkiv,[⊥] Farzad Mashayek,[⊥] Gabriel M. Veith,[*,○] Reza Shahbazian-Yassar,[*,⊥] and Raymond R. Unocic[*,§]

[†]Department of Materials Science and Engineering, Michigan Technological University, Houghton, Michigan 49931, United States
[‡]Universite Grenoble Alpes, CEA, LETI, MINATEC Campus, 38054 Grenoble, France
[§]Center for Nanophase Materials Sciences, Oak Ridge National Laboratory, Oak Ridge, Tennessee 37831, United States
[∥]Materials Science and Technology Division, Oak Ridge National Laboratory, Oak Ridge, Tennessee 37831, United States
[○]Chemical Sciences Division, Oak Ridge National Laboratory, Oak Ridge, Tennessee 37831, United States
[⊥]Department of Mechanical and Industrial Engineering, University of Illinois at Chicago, Chicago, Illinois 60607, United States

Supporting Information

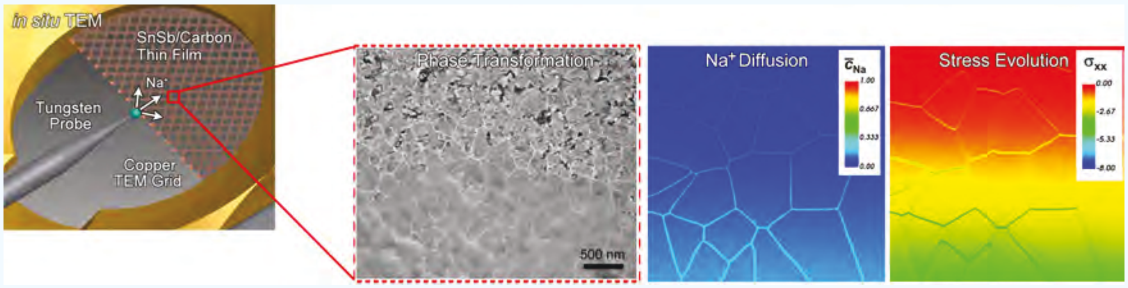

ABSTRACT: Intermetallic compounds such as SnSb are promising anode materials for sodium ion batteries; however, their nanoscale sodiation mechanisms are not well understood. Here, we used a combination of *in situ* transmission electron microscopy (TEM), first-principles electronic structure calculations, computational thermodynamic modeling, and phase-field simulations to reveal the sodiation mechanisms and to quantify microstructural effects contributing to the underlying reaction kinetics in SnSb electrodes. During *in situ* sodiation experiments, the nanocrystalline SnSb thin films underwent a rapid amorphous phase transformation upon sodiation, as determined by *in situ* TEM and electron diffraction experiments. The Na^+ diffusion coefficients were measured with and without an external electrical bias, and the data showed that an applied potential increased Na^+ diffusion by an order of magnitude compared to solid-state diffusion. Furthermore, there was a distinct decrease in sodium diffusion upon the formation of the amorphous phase that resulted from a change in the local structure and grain boundaries. To further understand how the Na^+ transport mechanism correlated with the changes observed in the SnSb thin films, phase-field modeling was used, which considered sodium diffusion within the grain boundaries together with their evolution and stress−strain state. These findings enhance our understanding of sodiation mechanisms within intermetallic anode materials for sodium ion battery applications.

KEYWORDS: *in situ transmission electron microscopy (TEM), sodium ion batteries, tin antimony, density functional theory, CALPHAD, phase-field simulations*

■ INTRODUCTION

Rechargeable sodium ion batteries (SIBs) are under consideration as an electrical energy storage solution for large-scale, stationary grid power storage applications due to their low cost, high energy density, and envisioned scalability.[1,2] As such, there has been a concerted research effort to explore suitable electrode chemistries that result in high energy density and prolonged cycled life at low voltages.[3] With respect to anode materials, tin (Sn), antimony (Sb), and the intermetallic SnSb are attractive candidate electrode materials because of their high theoretical storage capacities: 847 mAh g^{-1} (Sn),[4,5] 660 mAh g^{-1} (Sb),[6] and 752 mAh/g (SnSb),[7] assuming the formation of Na_3Sb and $Na_{15}Sn_4$ as end reaction products.

Complex sodiation mechanisms are inherent in these anode materials. For example, electrochemically prepared Na−Sn phases have been shown to adopt a number of unreported

Received: February 13, 2019
Accepted: April 16, 2019
Published: April 16, 2019

DOI: 10.1021/acsaem.9b00310

structures, with extensive Sn−Sn bonding at high sodium concentrations as determined from Mössbauer spectroscopy and nuclear magnetic resonance (NMR) measurements that compared line-compounds prepared by solid state reactions and electrochemically derived materials with similar Na−Sn ratios.[8−10] Analysis of the Mössbauer quadrupole splitting indicated that the Sn clusters are highly asymmetric due to the possible nonuniform migration of Sn/Na within the crystal structure. A similar variability in structural chemistry is observed for Na−Sb compounds, which form an amorphous Na−Sb structure for Na concentrations less than two. These multiphase reactions result in the formation of small domains of Na_3Sb and an unidentified Na−Sb compound.[8,11] In the case of intermetallic SnSb, X-ray diffraction (XRD) studies reveal that at maximum sodiation, the electrode remains mostly amorphous with a broad peak corresponding to Na_3Sb (confirmed by Mössbauer spectroscopy) and possibly a Na−Sn phase. Heating the end product to 95 °C results in the formation of crystalline Na_3Sb with no other crystalline Na−Sn phases found.[8] This is interesting since the reaction of pure Sn with Na results in a number of crystalline Na_xSn phases (x = 2.35 or x = 3.75).[4,5] These studies indicate that atomic diffusion within the Na−Sn−Sb structure is insufficient to achieve long-range crystallization of Na_3Sb and Na−Sn at room temperature. Given that the electrochemical formation of Na_3Sb occurs at a higher potential than Na−Sn suggests that Na^+ aggregates at the grain boundaries or within Na_3Sb domains, which may block diffusion pathways, spatially limit the crystallization of Na−Sn phases, or cause epitaxial strain that can inhibit the formation of Na−Sn domains.

To rationally design SIBs based on these anode chemistries, it is important to fundamentally understand the sodiation mechanisms and kinetics as they proceed at the nanoscale, through crystalline and amorphous phases. Such studies can strongly benefit from the use of high spatial resolution *in situ* transmission electron microscopy (TEM) methods.[12,13] *In situ* TEM has recently provided direct observations of structural and chemical changes within electrode materials and at electrode/electrolyte interfaces during ion intercalation,[14] alloying/dealloying,[15] conversion reaction,[16,17] solid electrolyte interphase formation,[18,19] or Li dendrite growth.[20−22] There have been several studies specific to SIBs, e.g., electrochemical sodiation in nanowires[23−29] and carbon,[30,31] but not for higher energy density intermetallics or under chemical diffusion. Here, we use a combination of *in situ* TEM and selected area electron diffraction (SAED) to study the phase change and to measure sodiation kinetics in SnSb thin films. The experimental results obtained were compared with thermodynamically stable structures using first-principles calculations based on density functional theory (DFT) and computational thermodynamic modeling (CALPHAD). Phase-field simulations were used to understand the sodiation transport mechanisms through grains and along grain boundaries in SnSb electrode material.

■ RESULTS AND DISCUSSION

Thermodynamic Modeling. The CALPHAD approach was used to investigate the thermodynamic phase stabilities of the Na−Sn−Sb ternary system in an effort to predict the sodiation reaction mechanisms and expected phases that should form within the SnSb system.[32] Thermodynamic descriptions for the constituent binaries were taken from the literature,[33−35] while the formation energies of two ternary phases, Na_5SnSb_3 and Na_8SnSb_4, were obtained from first-principles total energy calculations based on DFT. Perdew−Burke−Ernzerhof (PBE) exchange-correlation as implemented in the Vienna *Ab initio* Simulation Package (VASP) was used to calculate the total energies for pure elements and ternary phases.[36,37] The binary and ternary compounds considered in the present thermodynamic investigation are summarized in Table 1. All the solid phases were modeled as stoichiometric line compounds, except SnSb, to describe the phase field in the binary phase diagram. DFT results for the two ternary phases are presented in Table 2 and are in excellent agreement with experimental lattice parameters (within 1%). We incorporated the DFT-derived thermodynamic descriptions of the two ternary phases to the extrapolated binary thermodynamic descriptions.

Table 1. List of Binary and Ternary Solid Phases Considered in the Equilibrium Thermodynamic Phase Diagram

system	binary phases	ref
Na−Sn	$Na_{15}Sn_4$, Na_3Sn, Na_4Sn_3, Na_9Sn_4, $NaSn_3$, $NaSn_4$, $NaSn_6$, α-NaSn, β-NaSn	38
Na−Sb	Na_3Sb, NaSb	33
Sn−Sb	Sn_3Sb_2, SnSb	34
Na−Sn−Sb	Na_5SnSb_3, Na_8SnSb_4	

Table 2. DFT-Calculated Lattice Parameters of Na_5SnSb_3 and Na_8SnSb_4 Compared with Experiments[a]

phase	space group	exp	DFT	formation energy (kJ/mol)	ref
Na_5SnSb_3	$P1\ 2_1/C1$ (14)	a = 18.5940	a = 18.6565	−334.544	39
		b = 9.181	b = 9.270		
		c = 12.493	c = 12.399		
		α = 90°	α = 90°		
		β = 98.3°	β = 98.394°		
		γ = 90°	γ = 90°		
Na_8SnSb_4	$Fd\bar{3}m$ S (227)	a = 14.816	a = 14.8816	−515.200	40
		$\alpha = \beta = \gamma$ = 90°	$\alpha = \beta = \gamma$ = 90°		

[a] Reference states for formation energies of both ternary compounds are selected element reference, i.e., pure elements. Lattice parameters are given in Å.

From the complete thermodynamic modeling of Na−Sn−Sb, an isothermal section of Na−Sb−Sn at 25 °C was calculated, as shown in Figure 1a. Although both ternary phases have negative formation energies with respect to the pure elements, they do not appear in the calculated phase equilibria. As shown in Figure 1b, the formation enthalpies of both ternary phases lie slightly above the convex hull of Na/$SnSb_4$ and Na/$SnSb_3$, and the difference is 3.824 (Na_5SnSb_3) and 5.530 (Na_8SnSb_4) kJ/mol-atom, respectively. Hence, it can be postulated that Na_5SnSb_3 and Na_8SnSb_4 may participate in the sodiation reaction as metastable phases. However, Na_5SnSb_3 has a lower energy barrier compared to Na_8SnSb_4 and it is closer to SnSb in the Gibbs triangle. Thus, from a thermodynamic point-of-view, if Na_5SnSb_3 forms during the

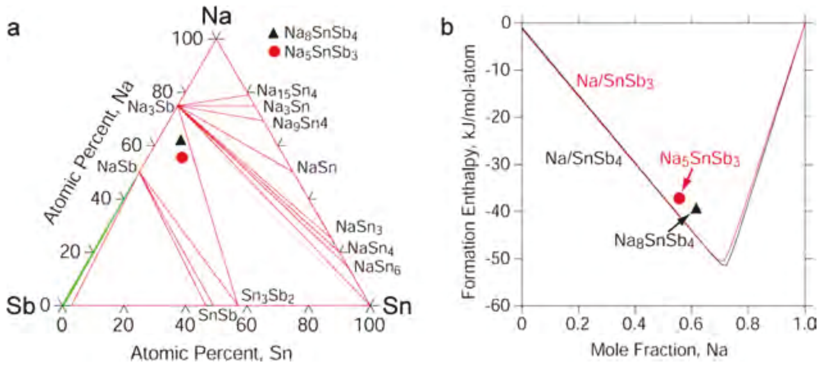

Figure 1. CALPHAD modeling of thermodynamically stable Na−Sn−Sb phases. Computed (a) isothermal section at 298.15 K (25 °C) and (b) formation enthalpies of Na-$SnSb_3$ and Na-$SnSb_3$ isopleths, from the evaluated thermodynamic description of Na−Sn−Sb with Na_5SnSb_3 and Na_8SnSb_4.

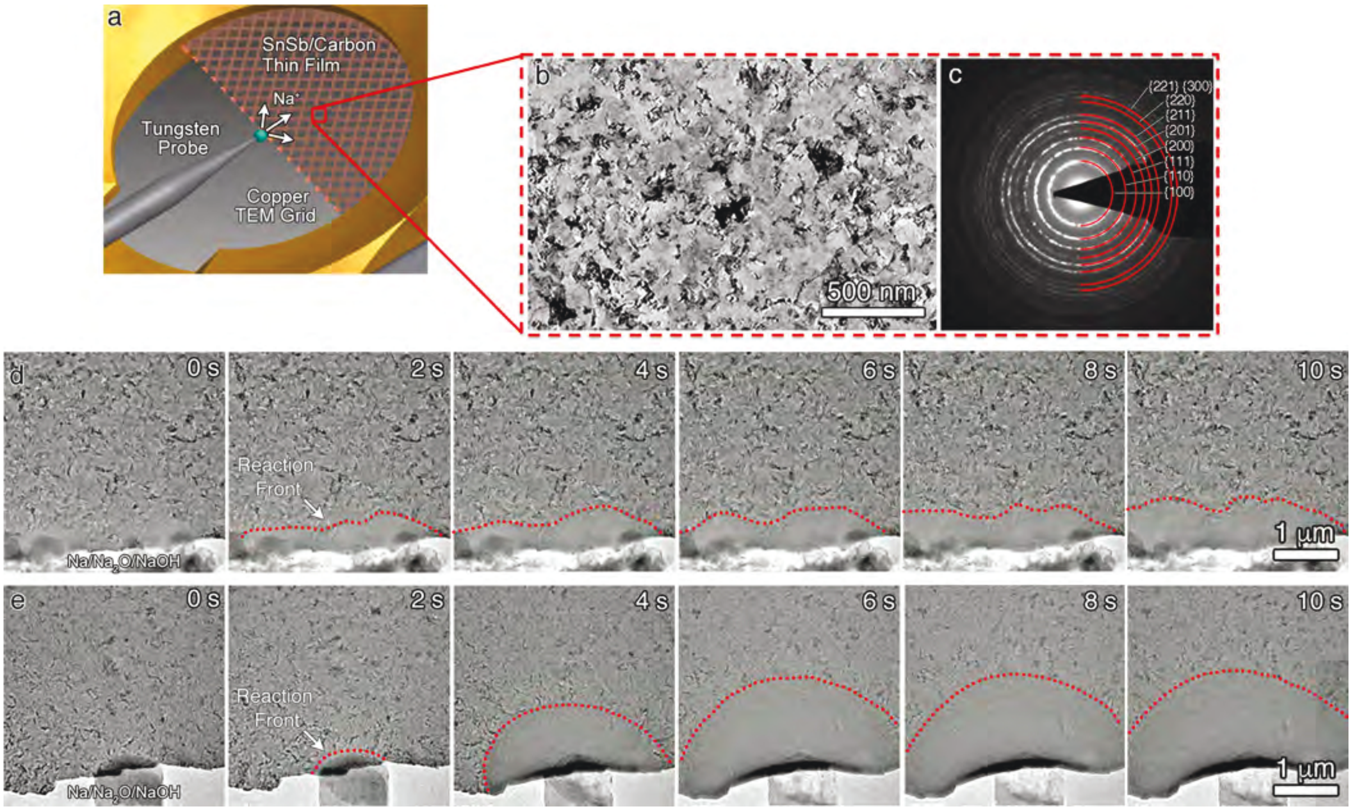

Figure 2. *In situ* TEM experiments. (a) Schematic of the *in situ* TEM platform used to monitor sodiation reaction mechanisms and kinetics in SnSb thin films. Inset (b) bright-field TEM image of RF magnetron sputtered SnSb thin film deposited onto an amorphous carbon TEM grid, with (c) a corresponding SAED ring pattern, indexed as pure SnSb. Bright-field TEM images comparing the sodiation of SnSb thin films under (d) chemical sodiation (no bias) and (e) electrochemical sodiation (−2 V vs Na/Na^+) conditions. Reaction front indicated highlighted by red dashed lines.

sodiation, it is expected to dominate the phase stabilities in equilibrium with adjacent binary constituents unless there is an excess amount of Na to allow the formation of Na_8SnSb_4.

***In Situ* Transmission Electron Microscopy.** *In situ* TEM sodiation experiments were performed using a commercial *in situ* TEM-STM electrical biasing holder (Nanofactory Instruments AB) in an FEI Titan scanning (S)/TEM operated at 300 kV. For the *in situ* sodiation experiments, electrochemical half-cells were constructed using an approach previously developed for *in situ* lithiation experiments of nanoparticles on amorphous carbon thin films.[16] A sodium metal counter electrode was fabricated by mounting a small amount of sodium metal onto an electropolished tungsten needle in an argon-filled glovebox. The sodium coated tungsten probe was brought into contact with the SnSb thin film using a piezo-driven biasing probe. The SnSb was deposited on amorphous carbon supported copper mesh TEM half-grids using radio frequency (RF) magnetron sputtering (Figure 2a) as described elsewhere.[41] The initial SnSb microstructure consisted of nanocrystalline grains, as shown in Figure 2b. The corresponding indexed SAED ring pattern in Figure 2c shows that the deposited thin film is composed of SnSb $R\bar{3}m$ phase (ICDD, PDF#00-033-0118). The structural and chemical evolution within the SnSb thin films during sodiation was captured via real-time TEM imaging and SAED. Due to unavoidable atmospheric exposure when transferring the *in situ* TEM

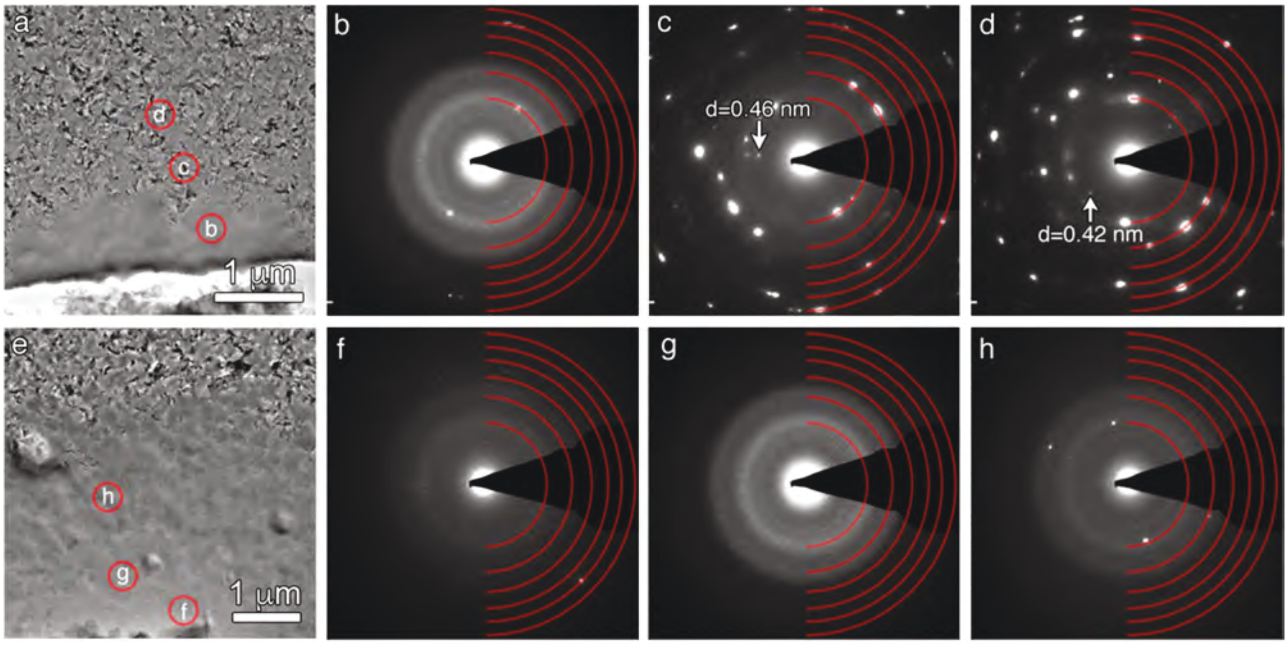

Figure 3. Phase identification. Bright-field TEM images and corresponding SAED patterns from site-specific regions in reacted SnSb thin films subjected to (a-d) chemical sodiation and (e-h) electrochemical sodiation. Red overlays in SAED patterns in (b-d) and (f-h) represent *d*-spacings for SnSb thin film prior to sodiation.

holder from the Ar-glovebox to the TEM, the sodium coated tungsten probe was passivated with Na_2O and/or NaOH, which effectively acted as a solid electrolyte. Two types of *in situ* TEM experiments were performed to distinguish the different phase transformations during sodiation: (1) solid-state chemical reaction and (2) electrochemical sodiation.

The time-lapsed bright-field TEM images used to distinguish between chemical vs electrochemical sodiation of the SnSb thin films are presented in Figures 2d and 2e, respectively. During chemical sodiation, e.g., no electrical bias applied, when the Na-coated tungsten probe contacted the SnSb, a reaction zone immediately formed. This zone is distinguishable from the unreacted, nanocrystalline SnSb film (Figure 2b) and the reaction front, marked by dashed lines, formed during the first few seconds after contact and spreads radially outward from the localized point of contact (refer to Movie S1 in the Supporting Information). The observed morphological changes in the wake of the reaction front is a clear indication that chemical sodiation in the SnSb thin film occurs. As the reaction proceeds, the source material is locally depleted of Na^+ ions, and it becomes more difficult to transport Na ions through the Na_2O/NaOH solid electrolyte, which serves to delay sodiation.

Faster sodiation is observed during electrochemical sodiation, e.g., under an applied bias, which is attributed to faster ion transport through the Na_2O/NaOH surface layer as a function of bias. The *in situ* electrochemical sodiation experiments were performed by applying −2 V vs Na/Na^+ from the source material to the SnSb thin film, which drives Na^+ transport. As shown in Figure 2e, a reaction front (marked by a dashed line) develops in a similar manner as during chemical sodiation; however, it occurs at a much faster rate. This is evident when comparing the TEM images/frames acquired at the same time intervals represented by the TEM images in the same column of Figures 2d-e. Electrochemical sodiation proceeds radially from the local point source of sodiation. The *in situ* observations (presented as Movie S2 in the Supporting Information) also reveal that the source material becomes locally depleted of Na^+, thereby causing a decrease in the rate at which Na^+ is transported through the Na_2O/NaOH solid electrolyte (similar to that observed during chemical sodiation). When the Na-loaded tungsten probe coated with Na_2O/NaOH is further brought into contact, we observe how Na^+ is transported through the sodiated SnSb. Visual comparison between the *in situ* chemical sodiation and electrochemical sodiation experiments shows that both reactions result in reaction zones that emanate radially from the point of contact, leading to grain restructuring and amorphous phase transformation, as evidenced by the electron diffraction data (discussed below). This restructuring agrees with the mechanisms proposed by Darwiche et al., where the first discharge is facile due to the decrease in grain sizes providing for an innately lower electrochemical potential.[42]

Phase Identification Using Selected Area Electron Diffraction. Selected area electron diffraction was used for phase identification during the chemical reaction experiments. Previous research has shown that structural phase transitions develop during sodiation of β-SnSb nanowires which results in an amorphous Na_xSn_y structure with crystalline Na_3Sb and $Na_{15}Sn_4$ phases.[43] The SAED results for our work are presented in Figure 3, which shows bright-field TEM images marked with the positions that indicate where SAED patterns were acquired. Each SAED pattern includes an overlay that corresponds to the as-deposited SnSb structure. The chemical sodiation results presented in Figures 3a-d show that sodiation of SnSb results in amorphization as indicated by the diffuse rings present in the SAED pattern (Figure 3b). Diffraction patterns were also acquired from regions close to the amorphous zone, and as indicated in subsequent SAED patterns, most of the diffraction spots corresponded to unreacted SnSb; however, an extra reflection with a *d*-spacing of 0.46 nm (Figure 3c) was identified, which is consistent with

DOI: 10.1021/acsaem.9b00310
ACS Appl. Energy Mater. 2019, 2, 3578−3586

Na_3Sb (d_{100}), Na_7Sn_3 (d_{101}) (also referred to as $Na_{5-x}Sn_2$), or $Na_{15}Sn_4$ (d_{220}). Similarly, from Figure 3d, several possible binary compounds are consistent with the reflection having a measured d-spacing of 0.42 nm: Na_3Sb (d_{101}), Na_7Sn_3 (d_{012}) (also referred to as $Na_{5-x}Sn_2$), or $Na_{15}Sn_4$ (d_{310}). The SAED patterns were acquired hundreds of nanometers away from the amorphous region, which suggests that Na^+ diffuses through the amorphous reaction zone. Similarly, SAED patterns were acquired from the electrochemically sodiated SnSb as presented in Figure 3e-h. All of the SAED patterns were acquired from within the sodiated region and exhibit the characteristic diffuse rings of an amorphous structure. The isolated diffraction spots in Figure 3f-h all correspond to unreacted SnSb. The phase identification results presented for both chemical and electrochemical sodiation reveal that sodiation in SnSb during *in situ* TEM result in a non-equilibrium amorphous phase transformation. These findings are different from that expected based on the equilibrium computational thermodynamic modeling results presented in Figure 1.

Sodiation Kinetic Measurements. The *in situ* TEM imaging experiments provide a unique opportunity to quantitatively analyze Na^+ transport by performing frame-by-frame, quantitative TEM image analysis to track changes in the size of the reaction zone as a function of the sodiation time. The distance from the Na^+ source contact point (the initiation site) to the reaction front boundary was approximated by fitting the area behind the reaction front with a cylindrical marker as a function of the elapsed time (t) of the reaction. The transformed area ($\langle x \rangle^2$) was calculated and divided in half to represent the sodiation reaction zone. It should be noted that the Na^+ source becomes depleted during the course of the experiment and eventually loses contact with the SnSb, which inhibits further Na^+ transport through the solid electrolyte layer. We also note that in the case of the chemical sodiation experiment, there were multiple, closely spaced initiation sites; thus, a single site encompassing the multiple sites was used for the data extraction.

Plotting $\langle x \rangle^2$ vs t (s) reveals significant differences between the electrochemical and chemical experiments, as shown in Figure 4, as well as a transition of the diffusion rate that occurs shortly after the onset of sodiation in both experiments. Fitting a linear curve to the data allows an estimated Na^+ diffusion coefficient (D) to be extracted at different stages of the reactions. The electrochemical experiment proceeds faster than the chemical experiment with D generally an order of magnitude greater, which is expected since the applied bias provides increased energy to drive the reaction. Nonetheless, these approximations appear to be in the proper range or are higher than comparative diffusivity values with respect to corollary tests with lithium and sodium.[44,45] After approximately 7 s, the reaction front transformation rate during the electrochemical experiment abruptly slows, where the diffusivity changes from an initial value of 8.1×10^{-9} $cm^2 \cdot s^{-1}$ to 7.9×10^{-10} $cm^2 \cdot s^{-1}$. Progression during the chemical experiment was similar; after 24 s, the diffusivity changes from 5.6×10^{-10} $cm^2 \cdot s^{-1}$ to 2.9×10^{-11} $cm^2 \cdot s^{-1}$. This difference in behavior during the course of the reaction experiments may be attributed to concomitant changes in microstructure during sodiation such as changes in grain size, grain boundary structure, and the crystalline to amorphous phase transformation.

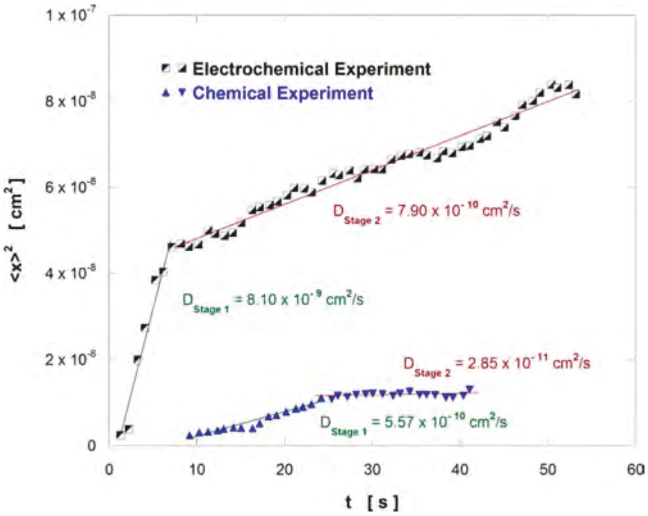

Figure 4. Sodium diffusion coefficient measurements. Plot of sodiated area ($\langle x \rangle^2$) vs time (t) from *in situ* TEM data (Figure 2) used to extract sodium diffusion coefficients (D) in SnSb during chemical (blue triangles) and electrochemical (black/white squares) biasing experiments.

The role of microstructural changes on Na^+ transport was further investigated by examining variables known to affect sodium diffusion, e.g., bulk diffusion within grains, grain boundary diffusion, and crystalline-to-amorphous/amorphous-to-crystalline phase transformations. The application of false color to a TEM image can be used to enhance the visualization of specific features and can be correlated with a representative schematic, as shown in Figure 5a. Acquired at the end of the electrochemical biasing experiment, the image shows the boundary between the amorphous and crystalline regions and grain boundaries (lighter blue) which are distinct evolving microstructural features that contribute to Na^+ diffusion. These changes correspond with an extremely fast sodiation process, designated as Stage 1, which is illustrated in the schematic shown in Figure 5a. The nanocrystalline SnSb grains are observed to transform within the reaction zone, from being essentially amorphous at the sodiation contact point to assuming larger grain sizes with well-defined grain boundaries at the reaction front boundary with the unaffected nanocrystalline SnSb. One might expect this grain restructuring to slow the overall ionic transport. Yet, the rate of Na^+ diffusivity continues to accelerate during Stage 1 indicating that the observed transitional structural changes likely enhance diffusion through the amorphous phase and grain boundaries. A variety of studies in similar battery materials provides further substantiation of these claims.[46−48] Amorphization initiates within grains following restructuring, as a facilitation of the alloying reactions, without hampering the observed diffusivity (Figure 5b). This makes sense upon considering the easier penetration of Na^+ into the smaller reconstructed grains, which have minimized bulk activation energies relative to their size, again, as an impact of lessened diffusion length. Amorphous materials are reported to have improved ionic transport attributed to a lack of long-range order (an associated form of free space), fluidity aspects of short-range pseudodefects with mechanistic similarities to vacancy and interstitial diffusion, meta-stability acting as reaction precursor, and local variances in energy barriers.[49] Overall, these factors generally allow for equivalent or faster ionic transport in

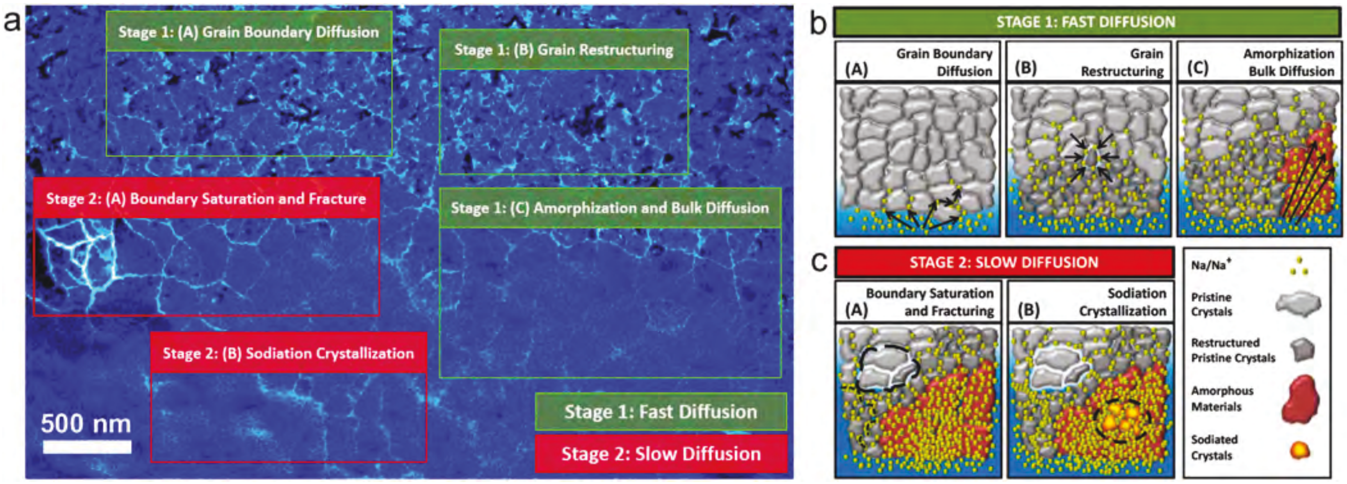

Figure 5. Microstructural evolution during sodiation in SnSb thin film anodes. a) TEM image showing various microstructural processes that account for Na^+ diffusion. Image is false colored to enhance visualization of grain boundaries. Annotations highlight different components of high diffusivity stage in the developed theory. b) Stage 1: (A-C) Schematics of potential diffusive mechanisms responsible for fast diffusion - grain boundary diffusion, grain restructuring, and amorphization, respectively. c) Stage 2: (A-B) Schematics for slow diffusion - boundary saturation with fracturing and crystallization of sodiated phases, respectively.

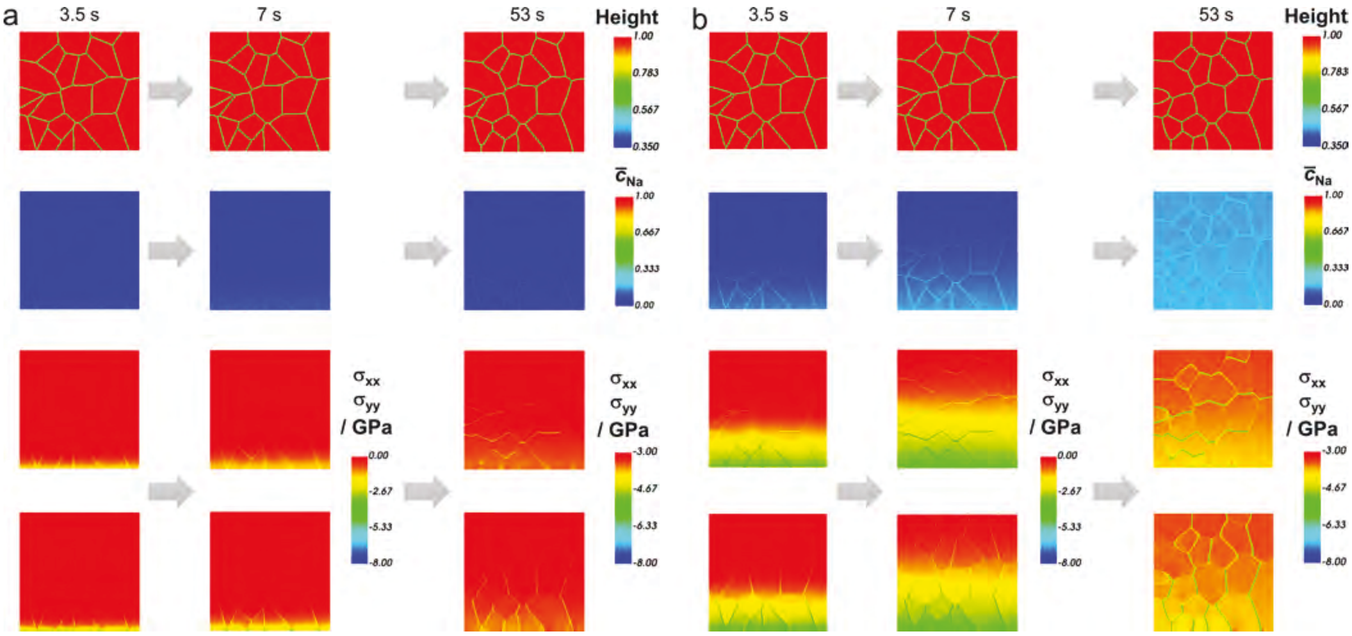

Figure 6. Phase-field simulation results. a) Chemical sodiation and b) electrochemical sodiation of SnSb electrodes. First upper panel depicts grain evolution in time (red color represents grains, yellow-green color represents grain boundaries), middle panel shows development of Na concentration in time along grain boundaries and grains; two lower panels show development of stress as a result of Na diffusion. Note: two different scales for stress depiction are chosen only for illustrative purposes to better visualize stress development in all directions.

amorphous phases compared to their crystalline counterparts in both traditional materials and battery materials.[50−53] More importantly, an applied electrical bias can supply abundant energy to overcome both grain boundary and bulk activation energies.

The examination of Stage 2 during the electrochemical reaction experiment elucidates the possible explanation for the measured shift in diffusion (Figure 5b). At a certain point in the highly reactive process of Stage 1, the grain boundaries begin to experience diminished ionic motion. This could be due to reaching a concentration saturation level or the formation of crystalline phases or volume strain effects. Indeed, as this saturation of the grain boundaries reaches maximal levels, the tendency for volumetric fracture becomes more probable; this is an undesirable outcome that can destroy conductive pathways on the bulk scale. Alongside this boundary expansion and fracturing, amorphous phases transition to a crystallized form that should yield less ionic flow.[54] Ongoing crystallization might also result in diffusion barriers developing at the grain boundaries, potentially in the form of pure metal nanodomains.[8,44] These barriers can inhibit the overall flow of the reactive Na^+, in effect global diffusivity, as the barriers require more energy to overcome, and result in the slower diffusion of sodium. This model may explain the apparent decrease in sodium diffusion within ZnO electrodes reported by Xu et al. which also showed a fast diffusion process followed by a second and third much slower process.[55]

Phase-Field Modeling of Sodiation in SnSb Thin Films. Phase-field modeling was used to further explore Na^+ transport through the SnSb thin films. It can be a challenge to experimentally link the real microstructural features observed within the nanocrystalline film electrodes with modeling and simulation results since the orientation, shape, and properties of each grain must be determined using grain orientation mapping over a large field-of-view. Furthermore, during RF magnetron sputtering of the SnSb thin films on the amorphous carbon film supported Cu TEM grid, defects and internal stresses can be generated that can change the initial stress state in the thin film prior to sodiation. For the current phase-field modeling, a grain structure is assumed to consist of an ideal set of randomly oriented grains with isotropic grain boundaries. Phase-field based numerical simulations were performed using the software package MOOSE. The procedure to solve differential equations used in the present modeling and simulation work is thoroughly described elsewhere.[56−58] Figure 6 shows the MOOSE-generated 2D polycrystalline microstructure of a SnSb electrode film employing the phase-field approach. The modeling domain used is 1 × 1 μm, and the Na source is positioned at the bottom allowing for 3D diffusion in any direction. There are three kinds of representations shown in Figure 6; the upper panel shows the grain boundary evolution with time, where the solid red color represents grains and yellow-green color signifies grain boundaries. The middle panel depicts the diffusion of Na along the grain boundaries. The lower panel shows the development of von Mises stress as a result of the progression of sodiation, and the single picture on the left shows the initial crystallographic orientation of each grain.

The initial grain structure was generated based upon the Voronoi tessellation approach, where the grain sizes remain in the range between 100 and 200 nm (as experimentally observed); correspondingly, the crystallographic orientation of each grain was randomly assigned by taking into account the number of grains. Grain growth was simulated based upon the isotropic grain boundary energy and grain boundary mobility assumptions. In addition, the grain boundary mobility is modeled as a function of the Na concentration. The migration front is much faster initially (two columns on left in Figure 6a) following sodium diffusion when compared to the later stage (last column in the second row), which is consistent with the experimental observation of the self-limiting sodiation process (Stage 1) (Figure 5). Furthermore, as sodiation progresses the formation of an amorphous phase at the bottom could be observed, where sodium diffuses not only within the grain boundaries but also within the amorphous structure.

To gain further insights into the sodiation induced grain restructuring process and amorphous phase transformation, we have also analyzed the stress state that is generated during the sodiation of the SnSb film. These results are shown in the lower panel of Figure 6. First, the stress is developed within the grain boundaries during the initial stage of sodiation, followed by an increase within the grains as amorphous phase is formed. As observed, a tensile stress develops in the sodiated regions; this tension originates from the sodiation-induced swelling of grain boundaries. As sodiation proceeds at the grain boundaries, the newly sodiated material tends to move in the outward direction, where the sodiation-induced volume expansion can be better accommodated with lower stresses generated large areas. Correspondingly, the areas with a small grain size and a significant tensile stress are more proned to volumetric fracturing compared to the large grains.

CONCLUSIONS

The sodiation mechanisms and kinetics in SnSb thin films have been studied through a combination of *in situ* TEM, CALPHAD modeling, and phase-field simulations in order to reveal the nanoscale origins of phase transformations associated with solid state chemical and electrochemical transformations. During sodiation, we find that the SnSb initially undergoes an amorphous phase transformation, which differs from the thermodynamic pathways that have been calculated using CALPHAD. By analyzing the sodiation reaction kinetics using quantitative image analysis, an initial fast sodium diffusion rate was found. However, the diffusivity decreases as sodium ions are transported through the amorphous phase, which limits the rate capability for this material system. These results are important as they provide microstructural insight into the ionic transport behavior of SnSb anodes that could support applications in rechargeable sodium ion batteries.

EXPERIMENTAL METHODS

Thin Film Synthesis. SnSb thin films were deposited onto a continuous carbon film supported on a 400 mesh copper TEM grid (Electron Microscopy Sciences CF-400-Cu) using DC magnetron sputtering from a SnSb target in pure Ar (99.99%, Air Liquide) at 20 mTorr pressure and 10 W DC power. Chamber pressure was 5×10^{-7} Torr or better. The target was prepared by ball-milling pure Sb (99.5%, Sigma-Aldrich) and Sn (99.9%, Alfa Aesar) powders with yittria-stabilized zirconia balls, pressing the recovered powder into a 2″ diameter disk, followed by annealing at 200 °C in flowing Ar for 40 h. Sputtered film thickness was estimated to be approximately 40 nm using a quartz microbalance installed inside the chamber. X-ray diffraction (XRD) was performed on the magnetron sputtering target and thicker films to ensure the formation of stoichiometric SnSb upon deposition, as documented in previous work.[8]

***In Situ* Microscopy.** A specialized scanning tunneling microscopy (STM) *in situ* TEM holder (Nanofactory Instruments) equipped with a piezo-driven probe/biasing nanomanipulator was used for the *in situ* TEM experiments. All holder preparations were conducted inside a positive pressure glovebox (Coy Laboratory Products) filled with ultrahigh purity argon (Ar) gas. TEM half-grids with the sputtered SnSb thin films specimens were loaded into the TEM holder. Sodium was then sourced onto an electropolished tungsten (W) probe tip by scratching a freshly exposed surface of bulk sodium metal. The probe was loaded into the piezo-motion side of the holder. The holder was then quickly transported to the FEI Titan S S/TEM (operating at 300 kV) for the *in situ* microscopy experiments. The brief exposure time during transport from the glovebox to the TEM column results in the formation of a sodium oxide/hydroxide layer on the surface of the sodium metal on the W tip which acts as a solid electrolyte and facilitates sodium ion transport during electrical biasing at −2 V vs Na/Na^+.

ASSOCIATED CONTENT

Supporting Information

The Supporting Information is available free of charge on the ACS Publications website at DOI: 10.1021/acsaem.9b00310.

Movie S1 (AVI)

Movie S2 (AVI)

AUTHOR INFORMATION

Corresponding Authors

*E-mail: veithgm@ornl.gov.
*E-mail: rsyassar@uic.edu.
*E-mail: unocicrr@ornl.gov.

ORCID

Xiahan Sang: 0000-0002-2861-6814
Vitaliy Yurkiv: 0000-0002-3407-891X
Gabriel M. Veith: 0000-0002-5186-4461
Raymond R. Unocic: 0000-0002-1777-8228

Notes

The authors declare no competing financial interest.

ACKNOWLEDGMENTS

Research at Oak Ridge National Laboratory (ORNL), managed by UT Battelle, LLC for the U.S. Department of Energy (DOE) under contract DE-AC05-00OR22725, was sponsored by the Office of Energy Efficiency and Renewable Energy, Vehicle Technologies Office (R.R.U.) and Office of Basic Energy Sciences, Division of Materials Sciences and Engineering. (L.B. and G.M.V.). DFT and CALPHAD calculations were performed by D.S., F.M., and V.Y. Financial support from NSF CBET-1805938 for the phase-field modeling work is acknowledged. R.S.Y. and J.G.K. efforts were supported by an NSF DMR-1620901 award. *In situ* microscopy and data analysis were conducted as part of a user project at ORNL's Center for Nanophase Materials Sciences, which is a U.S. DOE Office of Science User Facility.

REFERENCES

(1) Hwang, J.-Y.; Myung, S.-T.; Sun, Y.-K. Sodium-Ion Batteries: Present and Future. *Chem. Soc. Rev.* **2017**, *46*, 3529−3614.

(2) Kim, H.; Kim, H.; Ding, Z.; Lee, M. H.; Lim, K.; Yoon, G.; Kang, K. Recent Progress in Electrode Materials for Sodium-Ion Batteries. *Adv. Energy Mater.* **2016**, *6*, 1600943−38.

(3) Wang, L. P.; Yu, L.; Wang, X.; Srinivasan, M.; Xu, Z. J. Recent Developments in Electrode Materials for Sodium-Ion Batteries. *J. Mater. Chem. A* **2015**, *3*, 9353−9378.

(4) Ellis, L. D.; Hatchard, T. D.; Obrovac, M. N. Reversible Insertion of Sodium in Tin. *J. Electrochem. Soc.* **2012**, *159*, A1801−A1805.

(5) Baggetto, L.; Ganesh, P.; Meisner, R. P.; Unocic, R. R.; Jumas, J.-C.; Bridges, C. A.; Veith, G. M. Characterization of Sodium Ion Electrochemical Reaction with Tin Anodes: Experiment and Theory. *J. Power Sources* **2013**, *234*, 48−59.

(6) Darwiche, A.; Marino, C.; Sougrati, M. T.; Fraisse, B.; Stievano, L.; Monconduit, L. Better Cycling Performances of Bulk Sb in Na-Ion Batteries Compared to Li-Ion Systems: an Unexpected Electrochemical Mechanism. *J. Am. Chem. Soc.* **2012**, *134*, 20805−20811.

(7) Darwiche, A.; Sougrati, M. T.; Fraisse, B.; Stievano, L.; Monconduit, L. Facile Synthesis and Long Cycle Life of SnSb as Negative Electrode Material for Na-Ion Batteries. *Electrochem. Commun.* **2013**, *32*, 18−21.

(8) Baggetto, L.; Hah, H.-Y.; Jumas, J.-C.; Johnson, C. E.; Johnson, J. A.; Keum, J. K.; Bridges, C. A.; Veith, G. M. The Reaction Mechanism of SnSb and Sb Thin Film Anodes for Na-Ion Batteries Studied by X-Ray Diffraction, 119Sn and 121Sb Mössbauer Spectroscopies. *J. Power Sources* **2014**, *267*, 329−336.

(9) Baggetto, L.; Bridges, C. A.; Jumas, J.-C.; Mullins, D. R.; Carroll, K. J.; Meisner, R. A.; Crumlin, E. J.; Liu, X.; Yang, W.; Veith, G. M. The Local Atomic Structure and Chemical Bonding in Sodium Tin Phases. *J. Mater. Chem. A* **2014**, *2*, 18959−18973.

(10) Stratford, J. M.; Mayo, M.; Allan, P. K.; Pecher, O.; Borkiewicz, O. J.; Wiaderek, K. M.; Chapman, K. W.; Pickard, C. J.; Morris, A. J.; Grey, C. P. Investigating Sodium Storage Mechanisms in Tin Anodes: a Combined Pair Distribution Function Analysis, Density Functional Theory, and Solid-State NMR Approach. *J. Am. Chem. Soc.* **2017**, *139*, 7273−7286.

(11) Allan, P. K.; Griffin, J. M.; Darwiche, A.; Borkiewicz, O. J.; Wiaderek, K. M.; Chapman, K. W.; Morris, A. J.; Chupas, P. J.; Monconduit, L.; Grey, C. P. Tracking Sodium-Antimonide Phase Transformations in Sodium-Ion Anodes: Insights From Operando Pair Distribution Function Analysis and Solid-State NMR Spectroscopy. *J. Am. Chem. Soc.* **2016**, *138*, 2352−2365.

(12) Wang, C. In Situ Transmission Electron Microscopy and Spectroscopy Studies of Rechargeable Batteries Under Dynamic Operating Conditions: a Retrospective and Perspective View. *J. Mater. Res.* **2015**, *30*, 326−339.

(13) Yuan, Y.; Amine, K.; Lu, J.; Shahbazian-Yassar, R. Understanding Materials Challenges for Rechargeable Ion Batteries with in Situ Transmission Electron Microscopy. *Nat. Commun.* **2017**, *8*, 15806.

(14) Huang, J. Y.; Zhong, L.; Wang, C.; Sullivan, J. P.; Xu, W.; Zhang, L. Q.; Mao, S. X.; Hudak, N. S.; Subramanian, A.; Fan, H.; Qi, L.; Kushima, A.; Li, J. In Situ Observation of the Electrochemical Lithiation of a Single SnO2 Nanowire Electrode. *Science* **2010**, *330*, 1515−1520.

(15) McDowell, M. T.; Lee, S. W.; Harris, J. T.; Korgel, B. A.; Wang, C.; Nix, W. D.; Cui, Y. In Situ TEM of Two-Phase Lithiation of Amorphous Silicon Nanospheres. *Nano Lett.* **2013**, *13*, 758−764.

(16) Wang, F.; Yu, H.-C.; Chen, M.-H.; Wu, L.; Pereira, N.; Thornton, K.; Van der Ven, A.; Zhu, Y.; Amatucci, G. G.; Graetz, J. Tracking Lithium Transport and Electrochemical Reactions in Nanoparticles. *Nat. Commun.* **2012**, *3*, 1201−1208.

(17) Boebinger, M. G.; Xu, M.; Ma, X.; Chen, H.; Unocic, R. R.; McDowell, M. T. Distinct Nanoscale Reaction Pathways in a Sulfide Material for Sodium and Lithium Batteries. *J. Mater. Chem. A* **2017**, *5*, 11701−11709.

(18) Sacci, R. L.; Dudney, N. J.; More, K. L.; Parent, L. R.; Arslan, I.; Browning, N. D.; Unocic, R. R. Direct Visualization of Initial SEI Morphology and Growth Kinetics During Lithium Deposition by in Situ Electrochemical Transmission Electron Microscopy. *Chem. Commun.* **2014**, *50*, 2104−2104.

(19) Unocic, R. R.; Sun, X.-G.; Sacci, R. L.; Adamczyk, L. A.; Alsem, D. H.; Dai, S.; Dudney, N. J.; More, K. L. Direct Visualization of Solid Electrolyte Interphase Formation in Lithium-Ion Batteries with in Situ Electrochemical Transmission Electron Microscopy. *Microsc. Microanal.* **2014**, *20*, 1029−1037.

(20) Sacci, R. L.; Black, J. M.; Balke, N.; Dudney, N. J.; More, K. L.; Unocic, R. R. Nanoscale Imaging of Fundamental Li Battery Chemistry: Solid-Electrolyte Interphase Formation and Preferential Growth of Lithium Metal Nanoclusters. *Nano Lett.* **2015**, *15*, 2011−2018.

(21) Leenheer, A. J.; Jungjohann, K. L.; Zavadil, K. R.; Sullivan, J. P.; Harris, C. T. Lithium Electrodeposition Dynamics in Aprotic Electrolyte Observed in SituviaTransmission Electron Microscopy. *ACS Nano* **2015**, *9*, 4379−4389.

(22) Mehdi, B. L.; Qian, J.; Nasybulin, E.; Park, C.; Welch, D. A.; Faller, R.; Mehta, H.; Henderson, W. A.; Xu, W.; Wang, C. M.; Evans, J. E.; Liu, J.; Zhang, J.-G.; Muller, K. T.; Browning, N. D. Observation and Quantification of Nanoscale Processes in Lithium Batteries by Operando Electrochemical (S)TEM. *Nano Lett.* **2015**, *15*, 2168−2173.

(23) Xu, F.; Li, Z.; Wu, L.; Meng, Q.; Xin, H. L.; Sun, J.; Ge, B.; Sun, L.; Zhu, Y. In Situ TEM Probing of Crystallization Form-Dependent Sodiation Behavior in ZnO Nanowires for Sodium-Ion Batteries. *Nano Energy* **2016**, *30*, 771−779.

(24) Li, Z.; Tan, X.; Li, P.; Kalisvaart, P.; Janish, M. T.; Mook, W. M.; Luber, E. J.; Jungjohann, K. L.; Carter, C. B.; Mitlin, D. Coupling in Situ TEM and Ex Situ Analysis to Understand Heterogeneous Sodiation of Antimony. *Nano Lett.* **2015**, *15*, 6339−6348.

(25) Wang, J. W.; Liu, X. H.; Mao, S. X.; Huang, J. Y. Microstructural Evolution of Tin Nanoparticles During in Situ Sodium Insertion and Extraction. *Nano Lett.* **2012**, *12*, 5897−5902.

DOI: 10.1021/acsaem.9b00310
ACS Appl. Energy Mater. 2019, 2, 3578−3586

(26) Lu, X.; Adkins, E. R.; He, Y.; Zhong, L.; Luo, L.; Mao, S. X.; Wang, C.-M.; Korgel, B. A. Germanium as a Sodium Ion Battery Material: in SituTEM Reveals Fast Sodiation Kinetics with High Capacity. *Chem. Mater.* **2016**, *28*, 1236−1242.

(27) Li, Q.; Wang, P.; Feng, Q.; Mao, M.; Liu, J.; Mao, S. X.; Wang, H. In SituTEM on the Reversibility of Nanosized Sn Anodes During the Electrochemical Reaction. *Chem. Mater.* **2014**, *26*, 4102−4108.

(28) Nie, A.; Gan, L.-Y.; Cheng, Y.; Tao, X.; Yuan, Y.; Sharifi-Asl, S.; He, K.; Asayesh-Ardakani, H.; Vasiraju, V.; Lu, J.; Mashayek, F.; Klie, R. F.; Vaddiraju, S.; Schingenschlögl, U.; Shahbazian-Yassar, R. Ultrafast and Highly Reversible Sodium Storage in Zinc-Antimony Intermetallic Nanomaterials. *Adv. Funct. Mater.* **2016**, *26*, 543−552.

(29) Asayesh-Ardakani, H.; Yao, W.; Yuan, Y.; Nie, A.; Amine, K.; Lu, J.; Shahbazian-Yassar, R. In Situ TEM Investigation of ZnO Nanowires During Sodiation and Lithiation Cycling. *Small Methods* **2017**, *1*, 1700202−1700208.

(30) Liu, Y.; Fan, F.; Wang, J.; Liu, Y.; Chen, H.; Jungjohann, K. L.; Xu, Y.; Zhu, Y.; Bigio, D.; Zhu, T.; Wang, C. In Situ Transmission Electron Microscopy Study of Electrochemical Sodiation and Potassiation of Carbon Nanofibers. *Nano Lett.* **2014**, *14*, 3445−3452.

(31) Su, Q.; Du, G.; Zhang, J.; Zhong, Y.; Xu, B.; Yang, Y.; Neupane, S.; Li, W. In SituTransmission Electron Microscopy Observation of Electrochemical Sodiation of Individual Co 9S 8-Filled Carbon Nanotubes. *ACS Nano* **2014**, *8*, 3620−3627.

(32) Kaufman, L.; Bernstein, H. *Computer Calculation of Phase Diagram*; Academic Press, Inc.: New York, 1970.

(33) Liu, Y.; Xu, J.; Kang, Z.; Wang, J. Thermodynamic Descriptions and Phase Diagrams for Sb−Na and Sb−K Binary Systems. *Thermochim. Acta* **2013**, *569*, 119−126.

(34) Chen, S.-W.; Chen, C.-C.; Gierlotka, W.; Zi, A.-R.; Chen, P.-Y.; Wu, H.-J. Phase Equilibria of the Sn-Sb Binary System. *J. Electron. Mater.* **2008**, *37*, 992−1002.

(35) Wang, W.; Wang, S.; Jiao, H.; Zhan, P.; Jiao, S. A Sodium Ion Intercalation Material: a Comparative Study of Amorphous and Crystalline FePO4. *Phys. Chem. Chem. Phys.* **2015**, *17*, 4551−4557.

(36) Kresse, G.; Furthmiiller, J. Efficiency of Ab-Initio Total Energy Calculations for Metals and Semiconductors Using a Plane-Wave Basis Set. *Comput. Mater. Sci.* **1996**, *6*, 15−50.

(37) Kresse, G.; Furthmüller, J. Efficient Iterative Schemes for *Ab Initio* Total-Energy Calculations Using a Planse-Wave Basis Set. *Phys. Rev. B: Condens. Matter Mater. Phys.* **1996**, *54*, 11169−11186.

(38) Wang, J.; Miao, N.; Chartrand, P.; Jung, I.-H. Thermodynamic Evaluation and Optimization of the (Na+X) Binary Systems (X = Ag, Ca, in, Sn, Zn) Using Combined Calphad and First-Principles Methods of Calculation. *J. Chem. Thermodyn.* **2013**, *66*, 22−33.

(39) Eisenmann, B.; Klein, J. Na5SnSb3 Und K8SnSb4, Zwei Neue Zintlphasen Mit Tetraedrischen SnSb4-Baueinheiten. *Z. Naturforsch., B: J. Chem. Sci.* **1988**, *43*, 1156−1160.

(40) Eisenmann, B.; Klein, J. Eine Zintl-Phase Mit Isolierten SnSb4 8 -Anionen: Na8SnSb4. *Z. Naturforsch., B: J. Chem. Sci.* **1988**, *43*, 69−71.

(41) Baggetto, L.; Hah, H.-Y.; Jumas, J.-C.; Johnson, C. E.; Johnson, J. A.; Keum, J. K.; Bridges, C. A.; Veith, G. M. The Reaction Mechanism of SnSb and Sb Thin Film Anodes for Na-Ion Batteries Studied by X-Ray Diffraction, 119Sn and 121Sb Mössbauer Spectroscopies. *J. Power Sources* **2014**, *267*, 329−336.

(42) Darwiche, A.; Sougrati, M. T.; Fraisse, B.; Stievano, L.; Monconduit, L. Facile Synthesis and Long Cycle Life of SnSb as Negative Electrode Material for Na-Ion Batteries. *Electrochem. Commun.* **2013**, *32*, 18−21.

(43) Xie, H.; Tan, X.; Luber, E. J.; Olsen, B. C.; Kalisvaart, W. P.; Jungjohann, K. L.; Mitlin, D.; Buriak, J. M. B-SnSb for Sodium Ion Battery Anodes: Phase Transformations Responsible for Enhanced Cycling Stability Revealed by in Situ TEM. *ACS Energy Letters* **2018**, *3*, 1670−1676.

(44) Besenhard, J. O.; Wachtler, M.; Winter, M.; Andreaus, R.; Rom, I.; Sitte, W. Kinetics of Li Insertion Into Polycrystalline and Nanocrystalline "SnSb" Alloys Investigated by Transient and Steady State Techniques. *J. Power Sources* **1999**, *81−82*, 268−272.

(45) Ong, S. P.; Chevrier, V. L.; Hautier, G.; Jain, A.; Moore, C.; Kim, S.; Ma, X.; Ceder, G. Voltage, Stability and Diffusion Barrier Differences Between Sodium-Ion and Lithium-Ion Intercalation Materials. *Energy Environ. Sci.* **2011**, *4*, 3680−3689.

(46) Gu, M.; Kushima, A.; Shao, Y.; Zhang, J.-G.; Liu, J.; Browning, N. D.; Li, J.; Wang, C. Probing the Failure Mechanism of SnO 2Nanowires for Sodium-Ion Batteries. *Nano Lett.* **2013**, *13*, 5203−5211.

(47) Beaulieu, L. Y.; Larcher, D.; Dunlap, R. A.; Dahn, J. R. Reaction of Li with Grain-Boundary Atoms in Nanostructured Compounds. *J. Electrochem. Soc.* **2000**, *147*, 3206−3212.

(48) Pridatko, K. I. Electrochemical Insertion of Lithium in Thin Tin Films. *Russ. J. Electrochem.* **2006**, *42*, 63−70.

(49) Limoge, Y. Diffusion in Amorphous Materials. In *Diffusion in Materials*; Laskar, A. L., Bocquet, J. L., Brébec, G., Monty, C., Eds.; pp 601−624.

(50) Ding, N.; Xu, J.; Yao, Y. X.; Wegner, G.; Fang, X.; Chen, C. H.; Lieberwirth, I. Determination of the Diffusion Coefficient of Lithium Ions in Nano-Si. *Solid State Ionics* **2009**, *180*, 222−225.

(51) Duclot, M.; Souquet, J.-L. Glassy Materials for Lithium Batteries: Electrochemical Properties and Devices Performances. *J. Power Sources* **2001**, *97−98*, 610−615.

(52) Scaccia, S.; Carewska, M.; Wisniewski, P.; Prosini, P. P. Morphological Investigation of Sub-Micron FePO4 and LiFePO4 Particles for Rechargeable Lithium Batteries. *Mater. Res. Bull.* **2003**, *38*, 1155−1163.

(53) Tritsaris, G. A.; Zhao, K.; Okeke, O. U.; Kaxiras, E. Diffusion of Lithium in Bulk Amorphous Silicon: a Theoretical Study. *J. Phys. Chem. C* **2012**, *116*, 22212−22216.

(54) Wang, W.; Wang, S.; Jiao, H.; Zhan, P.; Jiao, S. A Sodium Ion Intercalation Material: a Comparative Study of Amorphous and Crystalline FePO 4. *Phys. Chem. Chem. Phys.* **2015**, *17*, 4551−4557.

(55) Xu, F.; Li, Z.; Wu, L.; Meng, Q.; Xin, H. L.; Sun, J.; Ge, B.; Sun, L.; Zhu, Y. In Situ TEM Probing of Crystallization Form-Dependent Sodiation Behavior in ZnO Nanowires for Sodium-Ion Batteries. *Nano Energy* **2016**, *30*, 771−779.

(56) Tonks, M. R.; Gaston, D.; Millett, P. C.; Andrs, D.; Talbot, P. An Object-Oriented Finite Element Framework for Multiphysics Phase Field Simulations. *Comput. Mater. Sci.* **2012**, *51*, 20−29.

(57) Gaston, D. R.; Permann, C. J.; Peterson, J. W.; Slaughter, A. E.; Andrš, D.; Wang, Y.; Short, M. P.; Perez, D. M.; Tonks, M. R.; Ortensi, J.; Zou, L.; Martineau, R. C. Physics-Based Multiscale Coupling for Full Core Nuclear Reactor Simulation. *Ann. Nucl. Energy* **2015**, *84*, 45−54.

(58) Yurkiv, V.; Gutiérrez-Kolar, J. S.; Unocic, R. R.; Ramsubramanian, A.; Shahbazian-Yassar, R.; Mashayek, F. Competitive Ion Diffusion Within Grain Boundary and Grain Interiors in Polycrystalline Electrodes with the Inclusion of Stress Field. *J. Electrochem. Soc.* **2017**, *164*, A2830−A2839.